Control Engineering Practice 76 (2018) 41–53

Contents lists available at ScienceDirect

Control Engineering Practice

journal homepage: www.elsevier.com/locate/conengprac

Adaptive-neural-network-based robust lateral motion control for autonomous vehicle at driving limits

Xuewu Ji [a], Xiangkun He [a], Chen Lv [b], Yahui Liu [a,*], Jian Wu [a]

[a] The State Key Laboratory of Automotive Safety and Energy, Tsinghua University, Beijing 100084, People's Republic of China
[b] Advanced Vehicle Engineering Center, Cranfield University, United Kingdom

ARTICLE INFO

Keywords:
Autonomous vehicle
Path tracking
Vehicle dynamics and control
Driving limits
Adaptive neural network
Backstepping variable structure control

ABSTRACT

Parametric modeling uncertainties and unknown external disturbance are major concerns in the development of advanced lateral motion controller for autonomous vehicle at the limits of driving conditions. Considering that tyre operating at or close to its physical limits of friction exhibits highly nonlinear force response and that unknown external disturbance can be caused by changing driving conditions, this paper presents a novel lateral motion control method that can maintain the yaw stability of autonomous vehicle while minimizing lateral path tracking error at the limits of driving conditions The proposed control scheme consists of a robust steering controller and an adaptive neural network (ANN) approximator. First, based on reference path model, dynamics model and kinematics model of vehicle, the robust steering controller is developed via backstepping variable structure control (BVSC) to suppress lateral path tracking deviation, to withstand unknown external disturbance and guarantee the yaw stability of autonomous vehicle. Then, by combining adaptive control mechanism based on Lyapunov stability theory and radial basis function neural network (RBFNN), the ANN approximator is designed to estimate uncertainty of tyre cornering stiffness and reduce its adverse effects by learning to approximate arbitrary nonlinear functions, and it ensures the uniform ultimate boundedness of the closed-loop system. Both simulation and experiment results show that the proposed control strategy can robustly track the reference path and at the same time maintains the yaw stability of vehicle at or near the physical limits of tyre friction.

1. Introduction

Vehicles have become an indispensable means of transportation in our present-day world, but the mobility brought by vehicles comes at a price (Eskandarian, 2012; Funke, Brown, Erlien, & Gerdes, 2017; He, Yang, Ji, Liu, & Deng, 2017; Zhang & Wang, 2017). In 2015, about 1.3 million people around the world are killed in traffic accidents, ranking tenth on the World Health Organization's list of top causes of death (World Health Organization, 2015). 72% of the traffic accidents can be traced to human error (Thomas, Morris, Talbot, & Fagerlind, 2013). With the rapid development of artificial intelligence and automobile technology, autonomous vehicle is expected to take more burden and stress from human driver, thus enhancing safety and reducing driver's workload, etc. (Brown, Funke, Erlien, & Gerdes, 2017; Lam, Leung, & Chu, 2016; Petrov & Nashashibi, 2014). Autonomous vehicle is a product of multi-disciplinary knowledge and theories, in which environment recognition system, decision-making system, motion control system are the three main components of the software system (González, Pérez, Milanés, & Nashashibi, 2016; Li, Chen, Li, Shaw, & Nuchter, 2014; Liu, Fan, Lv, et al., 2018). Many researchers have reported the progress made on overall architecture and the feasibility of autonomous vehicle technology (Gao, Gray, Tseng, & Borrelli, 2014; Kritayakirana & Gerdes, 2012a). This paper focuses on the motion control system of autonomous vehicle.

In designing the motion control scheme for autonomous vehicle, one of the most important considerations is to eliminate lateral path tracking error while ensuring vehicle stability during driving. In general, the motion control of autonomous vehicle can be achieved by longitudinal control and lateral control based on the information of current vehicle states and the road (Guo et al., 2017; Kim, Son, & Chung, 2016). Longitudinal control seeks to maintain a desired cruising speed and a safe distance between the leading vehicle and controlled vehicle for collision avoidance (Chen & Wang, 2011; Lefèvre, Carvalho, & Borrelli, 2016). Lateral control not only guides vehicles along the desired path, but also maintains vehicle stability. Therefore, it has become a hotspot for researchers. A linear time-varying model predictive control (MPC) which uses active front steering system in an autonomous vehicle is

* Corresponding author.
E-mail address: liuyahui@tsinghua.edu.cn (Y. Liu).

https://doi.org/10.1016/j.conengprac.2018.04.007
Received 9 September 2017; Received in revised form 11 April 2018; Accepted 13 April 2018

proposed to follow a given path in Falcone, Borrelli, Asgari, Tseng, and Hrovat (2007). Guo, Hu, Li, and Wang (2012) designed automatic steering controller for trajectory tracking of unmanned vehicles using genetic algorithms. Lee, Choi, Yi, Shin, and Ko (2014) focused on developing a hierarchical control algorithm for lane-keeping of vehicle using differential braking to prevent unintended lane departures. The local path tracking for autonomous vehicles was discussed using model predictive control (MPC) method, where the front wheel steering angle was used as the control variable, and the safety and actuator constraint factors were also considered (Yu, Guo, Sun, & Chen, 2015). The path following control for four-wheel independently actuated autonomous vehicles is designed through combining sliding model-based composite nonlinear feedback control of active front-wheel steering with direct yaw-moment control (Wang, Hu, Yan, & Chadli, 2016). An adaptive path tracking strategy for autonomous land vehicle based on neural dynamic programming is designed (Zhu, Huang, Liu, & Dai, 2016). To track the planned trajectory for collision avoidance maneuvers, the path-tracking controller formulated the tracking task as a multi-constrained model predictive control (MMPC) problem and calculated the front steering angle to prevent the vehicle from colliding with a moving vehicle (Ji, Khajepour, Melek, & Huang, 2017). A shared control algorithm using safe envelope of steering wheel angle is proposed to develop a human–machine cooperative steering system to avoid lane departure (Tan, Chen, Wang, & Gao, 2017). Hwang, Yang, and Hung (2017) presented a path tracking method of autonomous vehicle using hierarchically improved fuzzy dynamical sliding-model control.

However, as autonomous vehicles leave the research laboratory and enter public traffic, they must can react to emergency scenarios, some of which may necessitate maneuvering like in an emergency collision avoidance which happens in a short time horizon and requires large actuator inputs together with high yaw rates. Tyres will be highly saturated and begin to sideslip. In this situation, the characteristics of tyre force become highly nonlinear, which means the cornering force of tyre does not increase linearly with the increase of its slip angle, instead, it barely changes or even decreases with the increase of its slip angle. That is, vehicle is at the limits of driving conditions. The Dynamic Design Lab (DDL) in Stanford University has conducted a great deal of research for lateral motion control of autonomous vehicle in these conditions (Brown et al., 2017; Funke et al., 2017; Kapania & Gerdes, 2015; Kritayakirana & Gerdes, 2012a,b; Laurense, Goh, & Gerdes, 2017). In addition, several other researchers have also made important contribution in this area. In Rosolia, Carvalho, and Borrelli (2017), a learning nonlinear model predictive control is presented for autonomous racing problem that exploits information from previous laps to improve the performance of closed loop system over iterations. In Ni and Hu (2017), a hierarchical dynamics controller scheme is designed based on desired G–G diagram to push the autonomous vehicle to the driving limits on a given path, and the test of the controller is conducted based on an autonomous Formula SAE race car on an oval race track.

Although the above research achievements were successful to some extent, there are still two main challenges for lateral motion control of autonomous vehicle. Parametric modeling uncertainty and unknown external disturbance are of common occurrence in practical vehicle systems. If lateral tyre force in nonlinear region is treated as linear or driving environment changes abruptly, the behavior of the vehicle may become uncontrollable, and then autonomous vehicle will lose path tracking capability and stability. In the literature, though some researchers considered both parametric modeling uncertainty and unknown external disturbance in the design of lateral motion controller for autonomous vehicle, most of these researches do not focus on lateral motion control in the conditions of high lateral acceleration or low adhesion coefficient (Gao, Gray, Carvalho, Tseng, & Borrelli, 2014; Hang, Chen, Luo, & Fang, 2017; Hu, Jing, Wang, Yan, & Chadli, 2016; Kim et al., 2016; Ostafew, Schoellig, & Barfoot, 2016; Xia, Pu, Li, & Gao, 2016). As a matter of fact, in the linear region of tyres it is very easy to achieve good vehicle stability and controllability, which offers very limited scope for the consideration of parametric modeling uncertainty and disturbance on vehicle motion control.

Based on what has been mentioned above, it is necessary to investigate how to reduce the adverse effect of the parametric modeling uncertainty and unknown external disturbance on the lateral motion control of autonomous vehicle at the limits of driving conditions. The adaptive neural network (ANN) can effectively improve control performance against large uncertainty of system by learning to approximate arbitrary nonlinear functions, and the adaptation law is derived using Lyapunov function so that the stability and the convergence of the entire system are ensured (He, Chen, & Yin, 2016; Liu, 2013). However, there is the approximation error due to the employment of ANN, and the lateral motion control of autonomous vehicle should have strong robustness. The backstepping variable structure control (BVSC) is a specific type of robust control, which combines the merits of both backstepping control and those of variable structure control. This approach has shown its effectiveness in dealing with approximation error, multiple dynamics and mismatched uncertainties (Coban, 2017; Piltan, Mansoorzadeh, Zare, Shahryarzadeh, & Akbari, 2013). Nonetheless, this type of methods are developed on the basis of an assumed mathematical model, whose imperfections can lead to lowered performance of the controller. Hence, there is need to design some kind of compensator.

In the paper, a novel lateral motion control strategy is proposed to maintain yaw stability of autonomous vehicle while minimizing lateral path tracking deviation at the limits of driving conditions. The proposed control scheme consists of a robust steering controller and an ANN approximator. In the first stage, based on reference path model, dynamics model and kinematics model of vehicle, the robust steering controller is developed via the BVSC to suppress the lateral path tracking error, to withstand unknown external disturbance and ensure yaw stability for autonomous vehicle. In the second stage, by combining adaptive control mechanism based on Lyapunov stability theory and radial basis function neural network (RBFNN), ANN approximator is designed to compensate the uncertainty of tyre cornering stiffness by learning to approximate arbitrary nonlinear functions, and it guarantees the global asymptotic stability of the closed-loop system. Finally, a Matlab/Simulink–CarSim co-simulation and a test in hardware-in-the-loop (HIL) system are conducted to verify the effectiveness of the proposed lateral motion control method.

This paper is organized as follows: in Section 2 system models are built for controller design, including reference path model, vehicle kinematics model and vehicle dynamics model. In Section 3, the structure of the proposed control scheme is given, and a robust steering controller and an ANN approximator are designed. In Sections 4 and 5, the simulation results and experiment results are analyzed. Finally, the conclusion of this paper is made in Section 6.

2. System modeling for controller design

To design control law, the system models are developed in this section, which consist of reference path model, vehicle kinematics model, vehicle dynamics model.

2.1. Reference path model

This paper focuses on how to control the autonomous vehicle to maintain stabilization and track a reference path at the limits of driving conditions, so that the reference path will be given directly, without path planning.

The reference path model is described in terms of lateral position Y_{ref} and yaw angle ψ_{ref} as a function of the longitudinal position X (Falcone et al., 2007)

$$Y_{ref}(X) = \frac{d_{y_1}}{2}\left[1+\tanh\left(z_1\right)\right] - \frac{d_{y_2}}{2}\left[1+\tanh\left(z_2\right)\right], \quad (1)$$

$$\varphi_{ref}(X) = \arctan\left\{ d_{y_1}\left[\frac{1}{\cosh(z_1)}\right]^2\left(\frac{1.2}{d_{x_1}}\right) - d_{y_2}\left[\frac{1}{\cosh(z_2)}\right]^2\left(\frac{1.2}{d_{x_2}}\right)\right\}, \tag{2}$$

where $z_1 = (2.5/25)(X - 68) - 1.2$ or $(2.5/25)(X - 180) - 1.2$, $z_2 = (2.5/25)(X - 133) - 1.2$ or $(2.5/25)(X - 245) - 1.2$, $d_{x1} = 25$, $d_{x2} = 25$, $d_{y1} = 3.76$, and $d_{y2} = 3.76$.

2.2. Vehicle dynamics model

In order to consider vehicle dynamics characteristics in controller design, a two-degree-of-freedom (2DOF) vehicle dynamics model is adopted to capture the vehicle's essential lateral dynamics

$$\begin{cases} \dot{\beta} = \dfrac{F_{Lf} + F_{Lr}}{m v_x} - \gamma \\ \dot{\gamma} = \dfrac{a F_{Lf} - b F_{Lr}}{J_z} \end{cases}, \tag{3}$$

where β is sideslip angle of vehicle body, γ is yaw rate of vehicle body, m is the vehicle total mass, v_x is the longitudinal velocity, J_z is yaw moment of inertia, a and b are distance from the center of gravity to front-axle and rear-axle respectively, F_{Lf} and F_{Lr} are tyre lateral forces of front-axle and rear-axle respectively.

2.3. Vehicle kinematics model

To focus on path-tracking ability, the state variables of vehicle dynamics are transformed into state variables relevant to the reference path. Generally, it is desirable to eliminate both lateral error e and heading error $\Delta\psi$. But only one error can be reduced with single input steering angle δ_f. In this paper, the projected error e_p is adopted to combine the lateral error e and the heading error $\Delta\psi$. The vehicle kinematics model for the states in Fig. 1 is:

$$\begin{cases} \dot{e} = v_y \cos(\Delta\psi) + v_x \sin(\Delta\psi) \\ \dot{s} = v_x \cos(\Delta\psi) - v_y \sin(\Delta\psi) \\ e_p = e + x_p \sin(\Delta\psi) \\ \Delta\psi = \psi - \psi_r \end{cases}, \tag{4}$$

where v_y is lateral velocity, s is the distance along the reference path, ψ is the vehicle heading, ψ_r is the heading of the reference path, and x_p is the constant projected distance.

3. Lateral motion controller

In this section, the design of the proposed lateral motion controller is shown, which consists of a robust steering controller and an ANN approximator. A block diagram of the architecture for lateral motion controller is shown in Fig. 2. The robust steering controller is designed directly based on BVSC principle using reference path model, vehicle kinematics model and vehicle dynamics model. For the uncertainty of tyre cornering stiffness, an ANN approximator is proposed based on the adaptive mechanism and the RBFNN, which can approximate the uncertainty of unknown parameters and guarantee uniform ultimate boundedness of closed-loop system.

Because tyre–road information and vehicle states estimation schemes have already been discussed extensively in Ma et al. (2016), Liu, Li, Yang, Ji, and Wu (2017) and Hashemi et al. (2017), it is assumed that tyre–road friction coefficient, vehicle velocity and sideslip angle can be estimated directly, and other control data can be measured by environment recognition system or sensing system. In addition, the control of actuator, which is the steering motor, is not discussed in this study.

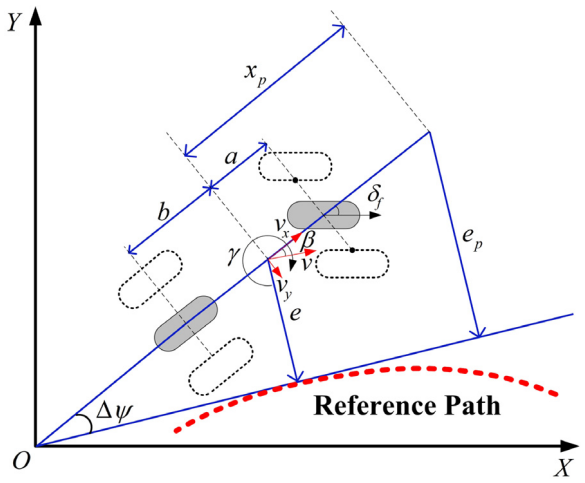

Fig. 1. Schematic of 2DOF vehicle dynamics model and vehicle kinematics model.

3.1. Robust steering controller design

According to small angle approximation for $\Delta\psi$, and by differentiating e_p and $\Delta\psi$ in Eq. (4), the following relations can be obtained:

$$\begin{cases} e_p = e + x_p \Delta\psi \\ \dot{e}_p = \dot{e} + x_p \Delta\dot{\psi} \\ \dot{e} = v_y + v_x \Delta\psi \\ \Delta\dot{\psi} = \dot{\psi} - \dot{\psi}_r = \gamma - K\dot{s}, \end{cases} \tag{5}$$

where K is the path curvature.

In the case of high lateral acceleration or low adhesion coefficient, the closed-loop steering response becomes underdamped, which results in significant oscillation of yaw rate (Kapania & Gerdes, 2015). In order to eliminate the projected error e_p and the oscillation of yaw rate, using Eq. (5), the following relations can be obtained:

$$\Delta\ddot{\psi} = \dot{\gamma} - \dot{K}\dot{s} - K\ddot{s}, \tag{6}$$

$$\ddot{e} = \dot{v}_y + \dot{v}_x \Delta\psi + v_x \Delta\dot{\psi}, \tag{7}$$

$$\begin{aligned} \ddot{e}_p &= \ddot{e} + x_p \Delta\ddot{\psi} \\ &= \dot{v}_y + \dot{v}_x \Delta\psi + v_x(\gamma - K\dot{s}) + x_p\left(\dot{\gamma} - \dot{K}\dot{s} - K\ddot{s}\right). \end{aligned} \tag{8}$$

Substitute Eq. (3) into Eq. (8), the following equation is obtained:

$$\ddot{e}_p = \dot{v}_y + \dot{v}_x \Delta\psi + v_x(\gamma - K\dot{s}) + x_p\left(\frac{a F_{Lf} - b F_{Lr}}{J_z} - \dot{K}\dot{s} - K\ddot{s}\right). \tag{9}$$

Considering that the effect of unknown external disturbance, the tyre lateral forces of front-axle and rear-axle can be described as

$$\begin{cases} F_{Lf} = F_{Cf} + d_f(\cdot) \\ F_{Lr} = F_{Cr} + d_r(\cdot) \end{cases}, \tag{10}$$

with

$$\begin{cases} F_{Cf} = \mu C_f \alpha_f \\ F_{Cr} = \mu C_r \alpha_r, \end{cases}$$

where F_{Cf} and F_{Cr} are tyre cornering force of front-axle and rear-axle respectively, $d_f(\cdot)$ and $d_r(\cdot)$ are lateral unknown external disturbances of front-axle and rear-axle respectively, α_f and α_r are tyre slip angles of front-axle and rear-axle respectively, C_f is tyre cornering stiffness of front-axle, C_r is tyre cornering stiffness of rear-axle, μ is tyre–road adhesion coefficient. Moreover, the tyre slip angles of front-axle and

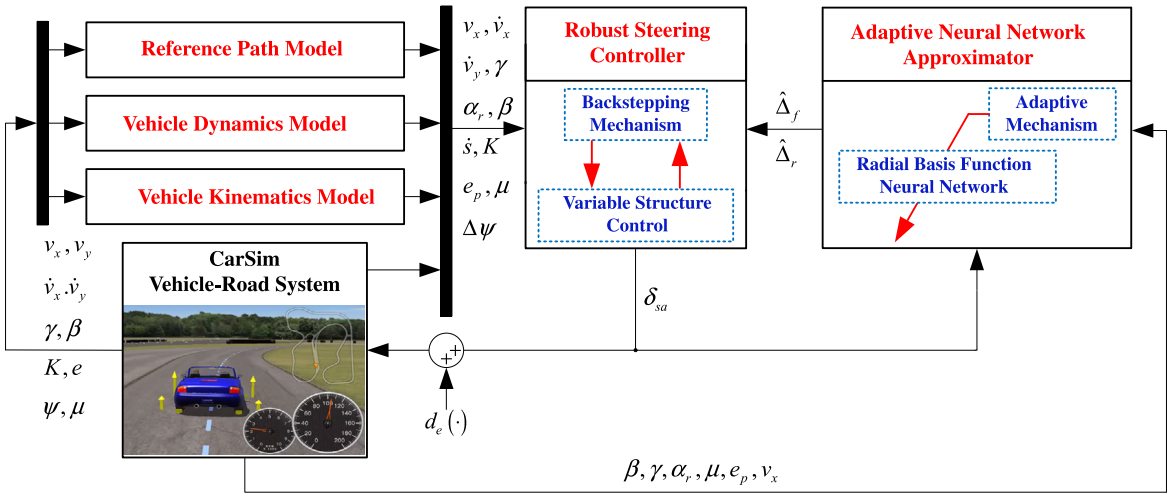

Fig. 2. Architecture of the proposed lateral motion controller for autonomous vehicle.

rear-axle can be described as:

$$\begin{cases} \alpha_f = \arctan\left[\dfrac{v\sin(\beta)+a\gamma}{v\cos(\beta)}\right]-\delta_f \approx \beta + a\dfrac{\gamma}{v_x}-\delta_f \\ \alpha_r = \arctan\left[\dfrac{v\sin(\beta)-b\gamma}{v\cos(\beta)}\right] \approx \beta - b\dfrac{\gamma}{v_x} \end{cases}, \tag{11}$$

where δ_f is front wheel steering angle, v is velocity of vehicle.

In order to fully consider the nonlinear cornering characteristics of tyre, the cornering stiffness can be defined as:

$$\begin{cases} C_f = C_{fo} + \Delta_f \\ C_r = C_{ro} + \Delta_r \end{cases}, \tag{12}$$

where C_{f0} and C_{r0} are nominal cornering stiffnesses of front-axle and rear-axle, Δ_f and Δ_r are uncertainties for tyre cornering stiffness of front-axle and rear-axle respectively.

Combining Eqs. (9)–(11), a nonlinear vehicle–road system model is obtained:

$$\begin{cases} \ddot{e}_p = q_1 + q_2 + q_3\delta_f + x_p\dfrac{ad_f(\cdot)-bd_r(\cdot)}{J_z} \\ q_1 = \dot{v}_y + \dot{v}_x\Delta\psi + v_x(\gamma - K\dot{s}) \\ q_2 = x_p\left[\dfrac{\mu a\left(v_x\beta + a\gamma\right)C_f}{v_x J_z} - \dfrac{\mu b\alpha_r C_r}{J_z} - \dot{K}\dot{s} - K\ddot{s}\right] \\ q_3 = -x_p\dfrac{\mu a C_f}{J_z} \end{cases}, \tag{13}$$

where q_1, q_2 and q_3 are system variables.

As shown in Eq. (13), the unknown external disturbance influences the lateral motion control performance of autonomous vehicle by forming yaw moment. Therefore, to simplify the design of the controller, and to conveniently analyze the unknown external disturbance's influence on lateral motion control performance of autonomous vehicle, the unknown external disturbance can be transformed into random input for front wheel angle or steering actuator, and then the following relation can be defined as:

$$d_{fe}(\cdot) = q_3\frac{d_e(\cdot)}{i} = x_p\frac{ad_f(\cdot)-bd_r(\cdot)}{J_z}, \tag{14}$$

with

$$\left|d_{fe}(\cdot)\right| \le D,$$

where $d_{fe}(\cdot)$ is equivalent random disturbance acting on front-axle of vehicle, $d_e(\cdot)$ is equivalent random disturbance acting on steering actuator, i is steering ratio, D is a positive constant.

Hence, under the equivalent random disturbance, Eq. (13) can be transformed into the following form:

$$\begin{cases} \dot{x}_1 = x_2 \\ \dot{x}_2 = q_1 + q_2 + q_3\delta_f + d_{fe}(\cdot) \end{cases}, \tag{15}$$

where $x_1 = e_p$.

In the following part, the BVSC design procedure for system (15) is given.

Step 1. With Eq. (15), the tracking error e_1 and its corresponding first order derivative are defined as:

$$\begin{cases} x_d = 0 \\ e_1 = x_1 - x_d = x_1 \\ \dot{e}_1 = \dot{x}_1 - \dot{x}_d = x_2 \end{cases}, \tag{16}$$

where x_d is the desired value.

To make the tracking error e_1 converge to zero, design Lyapunov function as:

$$V_1 = \frac{1}{2}e_1^2. \tag{17}$$

Therefore, the differentiation of Eq. (17) is derived:

$$\dot{V}_1 = e_1\dot{e}_1. \tag{18}$$

In order to achieve $\dot{V}_1 \le 0$, the switching surface function is defined as:

$$\begin{aligned} S_f &= x_2 + c_1x_1, \\ &= \dot{e}_1 + c_1e_1, \end{aligned} \tag{19}$$

where c_1 is a strictly positive gain parameter.

With Eq. (19), Eq. (18) can be written as:

$$\dot{V}_1 = e_1S_f - c_1e_1^2. \tag{20}$$

If $S_f = 0$, then $\dot{V}_1 \le 0$. Therefore, the design of next step is required.

Step 2. Select Lyapunov function can be written as:

$$V_2 = V_1 + \frac{1}{2}S_f^2. \tag{21}$$

Combining Eqs. (15) and (19), differentiation of the switching surface function can be derived:

$$\begin{aligned} \dot{S}_f &= \dot{x}_2 + c_1\dot{e}_1 \\ &= q_1 + q_2 + q_3\delta_f + d_{fe}(\cdot) + c_1\dot{e}_1. \end{aligned} \tag{22}$$

The derivative of V_2 becomes:

$$\begin{aligned} \dot{V}_2 &= \dot{V}_1 + S_f\dot{S}_f \\ &= e_1S_f - c_1e_1^2 + S_f\left[q_1 + q_2 + q_3\delta_f + d_{fe}(\cdot) + c_1\dot{e}_1\right]. \end{aligned} \tag{23}$$

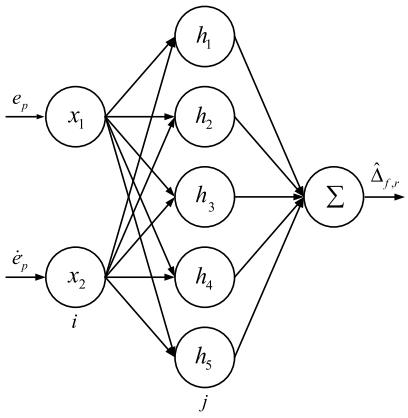

Fig. 3. The structure of adopted RBFNN.

In order to implement $\dot{V}_2 \le 0$, a stabilizing control law is designed:

$$\delta_f = -\frac{q_1 + q_2 + e_1 + c_1\dot{e}_1 + c_2 S_f + \eta \tanh\left(S_f\right)}{q_3}, \tag{24}$$

where c_2 is the strictly positive gain parameter, and the appropriate strictly positive gain factor η can be designed, for instance, this work is able to select:

$$\eta \gg D. \tag{25}$$

Substitute Eq. (24) into Eq. (23), according to Eq. (25) and Appendix A, the following relation can be obtained:

$$\dot{V}_2 = -c_1 e_1^2 - c_2 S_f^2 - \eta S_f \tanh\left(S_f\right) + S_f d_{fe}(\cdot) \le 0. \tag{26}$$

Therefore, $x_1 \to 0$, $x_2 \to 0$ and $S_f \to 0$ as $t \to \infty$.

3.2. Adaptive neural network approximator

At or close to driving limits, the tyre shows highly nonlinear force response, and the tyre cornering stiffness exhibits strong uncertainty, making it difficult to implement the control law δ_f (24). Therefore, the ANN approximator is used to adaptively learn the uncertainty of tyre cornering stiffness. In this ANN approximator, adaptive control theory and RBFNN are used to estimate uncertainty of tyre cornering stiffness. Fig. 2 shows the adaptive mechanism-based neural network approximator scheme. The structure of adopted RBFNN is a three-layer feedforward network shown as in Fig. 3. The input layer is a set of source nodes. The second layer is a hidden layer of high dimension. The output layer gives the response of the network to the activation patterns applied to the input layer (Fei & Ding, 2012).

The algorithm of RBFNN is:

$$h_j = \exp\left(\frac{\left\|x - c_j\right\|^2}{2b_j^2}\right), \tag{27}$$

$$\begin{cases} \Delta_f(\cdot) = W^{*\mathrm{T}} h_f(x) + \varepsilon_f \\ \Delta_r(\cdot) = V^{*\mathrm{T}} h_r(x) + \varepsilon_r \end{cases}, \tag{28}$$

$$x = [e_p \quad \dot{e}_p]^{\mathrm{T}}, \tag{29}$$

where i is the input number of the network, j is the number of hidden layer nodes in the network, x is input of the network, $h_{f,r} = [h_j]^{\mathrm{T}}$ is the output of Gaussian function, c_j is the center vector of neural net j, b_j represents the width value of Gaussian function for neural net j, W^* and V^* are the ideal neural network weights, $\varepsilon_{f,r}$ is approximation error of the neural network, and $|\varepsilon_{f,r}| \le \varepsilon_{\mathrm{N}}$, the items $C_{f,r}(.)$ is the ideal output value of the network.

Define the RBF neural network's learning indicator as:

$$E = \frac{1}{2} e_p^2. \tag{30}$$

According to gradient descent method, the learning algorithm of neural network weights (the base width vector, the center vector) can be obtained as:

$$\begin{aligned} db_j &= -\rho \frac{\partial E}{\partial b_j} = -\rho e_p W_j h_j \frac{\left\|x - c_j\right\|^2}{b_j^3} \\ b_j(t+1) &= b_j(t) + db_j + \zeta\left[b_j(t) - b_j(t-1)\right] \end{aligned}, \tag{31}$$

$$\begin{aligned} dc_{ij} &= -\rho \frac{\partial E}{\partial c_{ij}} = -\rho e_p W_j h_j \frac{x_i - c_{ij}}{b_j^2} \\ c_{ij}(t+1) &= c_{ij}(t) + dc_{ij} + \zeta\left[c_{ij}(t) - c_{ij}(t-1)\right] \end{aligned}, \tag{32}$$

where $\rho \in (0, 1)$ is the learning rate and $\zeta \in (0, 1)$ is momentum factor.

Using the gradient descent method to design the weights adjustment law W and V of RBFNN, only local optimization can be achieved, the closed-loop system stability cannot be guaranteed, and the closed-loop system control is easy to diverge (Liu, 2013). To solve this problem, the adaptive law is designed based on Lyapunov stability theory, and the closed-loop system stability can be guaranteed. The output of RBFNN is:

$$\begin{cases} \hat{\Delta}_f(x) = \hat{W}^{\mathrm{T}} h_f(x) \\ \hat{\Delta}_r(x) = \hat{V}^{\mathrm{T}} h_r(x) \end{cases}, \tag{33}$$

where $\hat{W}$ and $\hat{V}$ are the estimated RBFNN weights.

Accordingly, Eq. (12) can be written as:

$$\begin{cases} \hat{C}_f = C_{fo} + \hat{\Delta}_f \\ \hat{C}_r = C_{ro} + \hat{\Delta}_r \end{cases}, \tag{34}$$

To simplify the mathematical derivation, the following parameter matrix is defined

$$P = \begin{bmatrix} p_{11} & p_{12} \\ p_{21} & p_{22} \end{bmatrix} = \begin{bmatrix} \dfrac{\mu a x_p \left(v_x \beta + a\gamma\right)}{v_x J_z} & -\dfrac{\mu b \alpha_r x_p}{J_z} \\ -x_p\left(\dot{K}\dot{s} + K\ddot{s}\right) & -\dfrac{\mu a x_p}{J_z} \end{bmatrix}. \tag{35}$$

Therefore, combining Eqs. (13), (34) and (35), the control law δ_f (24) can be described as:

$$\delta_f = -\frac{q_1 + p_{11}\hat{C}_f + p_{12}\hat{C}_r + p_{21} + e_1 + c_1\dot{e}_1 + c_2 S_f + \eta \tanh\left(S_f\right)}{p_{22}\hat{C}_f}. \tag{36}$$

The control law δ_f is replaced with Eq. (36), and combining Eqs. (13), (34) and (35), Eq. (22) can be written as:

$$\begin{aligned} \dot{S}_f &= q_1 + q_2 + q_3\delta_f + c_1\dot{e}_1 + d_{fe}(\cdot) \\ &= q_1 + p_{11}\left(C_{f0} + \Delta_f\right) + p_{12}\left(C_{r0} + \Delta_r\right) + p_{21} + q_3\delta_f + c_1\dot{e}_1 + d_{fe}(\cdot) \\ &= q_1 + p_{11}\left(C_{f0} + \Delta_f\right) + p_{12}\left(C_{r0} + \Delta_r\right) + p_{21} + p_{22}\left(C_{f_0} + \hat{\Delta}_f\right)\delta_f \\ &\quad + \left[q_3 - p_{22}\left(C_{f_0} + \hat{\Delta}_f\right)\right]\delta_f + c_1\dot{e}_1 + d_{fe}(\cdot) \\ &= \left(p_{11} + p_{22}\delta_f\right)\left(\Delta_f - \hat{\Delta}_f\right) + p_{12}\left(\Delta_r - \hat{\Delta}_r\right) - e_1 - c_2 S_f \\ &\quad -\eta \tanh\left(S_f\right) + d_{fe}(\cdot). \end{aligned} \tag{37}$$

Define the differences between the ideal and the estimated RBFNN weights as:

$$\begin{cases} \widetilde{W} = W^* - \hat{W} \\ \widetilde{V} = V^* - \hat{V}. \end{cases} \tag{38}$$

With Eqs. (28) and (33), the following equations can be obtained:

$$\begin{cases} \widetilde{\Delta}_f = \Delta_f - \hat{\Delta}_f = W^{*\mathrm{T}} h_f(x) + \varepsilon_f - \hat{W}^{\mathrm{T}} h_f(x) = \widetilde{W}^{\mathrm{T}} h_f(x) + \varepsilon_f \\ \widetilde{\Delta}_r = \Delta_r - \hat{\Delta}_r = V^{*\mathrm{T}} h_r(x) + \varepsilon_r - \hat{V}^{\mathrm{T}} h_r(x) = \widetilde{V}^{\mathrm{T}} h_r(x) + \varepsilon_r. \end{cases} \tag{39}$$

Select the Lyapunov function as:

$$V_3 = V_2 + \frac{1}{2k_1}\widetilde{W}^{\mathrm{T}}\widetilde{W} + \frac{1}{2k_2}\widetilde{V}^{\mathrm{T}}\widetilde{V}, \tag{40}$$

where k_1 and k_2 are positive gain parameters.

With Eqs. (37)–(39), the corresponding first derivative of V_3 becomes:

$$\begin{aligned}
\dot{V}_3 &= \dot{V}_2 + \frac{1}{k_1}\widetilde{W}^{\mathrm{T}}\dot{\widetilde{W}} + \frac{1}{k_2}\widetilde{V}^{\mathrm{T}}\dot{\widetilde{V}} \\
&= e_1 S_f - c_1 e_1^2 + \frac{1}{k_1}\widetilde{W}^{\mathrm{T}}\dot{\widetilde{W}} + \frac{1}{k_2}\widetilde{V}^{\mathrm{T}}\dot{\widetilde{V}} + S_f \dot{S}_f \\
&= e_1 S_f - c_1 e_1^2 - \frac{1}{k_1}\widetilde{W}^{\mathrm{T}}\dot{\hat{W}} - \frac{1}{k_2}\widetilde{V}^{\mathrm{T}}\dot{\hat{V}} + S_f\left[\left(p_{11} + p_{22}\delta_f\right)\widetilde{\Delta}_f \right. \\
&\quad \left. + p_{12}\widetilde{\Delta}_r - e_1 - c_2 S_f - \eta \tanh\left(S_f\right) + d_{fe}(\cdot)\right] \\
&= e_1 S_f - c_1 e_1^2 - \frac{1}{k_1}\widetilde{W}^{\mathrm{T}}\dot{\hat{W}} - \frac{1}{k_2}\widetilde{V}^{\mathrm{T}}\dot{\hat{V}} \\
&\quad + S_f\left\{\left(p_{11} + p_{22}\delta_f\right)\left[\widetilde{W}^{\mathrm{T}}h_f(x) + \varepsilon_f\right] + p_{12}\left[\widetilde{V}^{\mathrm{T}}h_r(x) + \varepsilon_r\right]\right. \\
&\quad \left. - e_1 - c_2 S_f - \eta \tanh\left(S_f\right) + d_{fe}(\cdot)\right\} \\
&= -c_1 e_1^2 - c_2 S_f^2 - \eta S_f \tanh\left(S_f\right) + S_f\left[\left(p_{11} + p_{22}\delta_f\right)\varepsilon_f \right. \\
&\quad \left. + p_{12}\varepsilon_r + d_{fe}(\cdot)\right] \\
&\quad + \widetilde{W}^{\mathrm{T}}\left[\left(p_{11} + p_{22}\delta_f\right)S_f h_f(x) - \frac{\dot{\hat{W}}}{k_1}\right] + \widetilde{V}^{\mathrm{T}}\left[p_{12}S_f h_r(x) - \frac{\dot{\hat{V}}}{k_2}\right].
\end{aligned} \tag{41}$$

Let adaptive law be:

$$\begin{cases}
\dot{\hat{W}} = k_1\left(p_{11} + p_{22}\delta_f\right)S_f h_f(x) \\
\dot{\hat{V}} = k_2 p_{12} S_f h_r(x).
\end{cases} \tag{42}$$

Substituting Eq. (42) into Eq. (41), the following relation can be derived:

$$\begin{aligned}
\dot{V}_3 &= -c_1 e_1^2 - c_2 S_f^2 - \eta S_f \tanh\left(S_f\right) \\
&\quad + S_f\left[\left(p_{11} + p_{22}\delta_f\right)\varepsilon_f + p_{12}\varepsilon_r + d_{fe}(\cdot)\right].
\end{aligned} \tag{43}$$

Due to the fact that approximation errors ε_f and ε_r are limited and sufficiently small, the appropriate and strictly positive gain factor η can be selected, for instance, it is designed as:

$$\eta \gg \left|\left(p_{11} + p_{22}\delta_f\right)\varepsilon_f + p_{12}\varepsilon_r\right| + D. \tag{44}$$

And then, the following inequality can be obtained:

$$\dot{V}_3 \leq 0, \tag{45}$$

in which case the closed-loop system is robust globally asymptotically stable.

With Eq. (36), the control input for steering actuator can be written as:

$$\delta_{sa} = i\delta_f. \tag{46}$$

In addition, the estimated tyre lateral forces of front-axle and rear-axle can be described as:

$$\begin{cases}
\hat{F}_{Lf} = \mu\hat{C}_f\left[\beta + a\dfrac{\gamma}{v_x} - \delta_f - \dfrac{d_e(\cdot)}{i}\right] \\
\hat{F}_{Lr} = \mu\hat{C}_r\left(\beta - b\dfrac{\gamma}{v_x}\right).
\end{cases} \tag{47}$$

For the RBFNN, the initial parameters of the Gaussian function b_0 and c_0 are chosen as 5 and $\begin{bmatrix} -1 & -0.5 & 0 & 0.5 & 1 \\ -5 & -2.5 & 0 & 2.5 & 5 \end{bmatrix}$, and the initial weight value is chosen as zero. Moreover, in this paper, the other key parameters of the lateral motion controller are given in Table 1.

4. Simulation and discussions

In this section, according to the parameters of the experimental vehicle in our laboratory, the experimental verification of the vehicle model is conducted to obtain an accurate simulation model, and then two simulation cases are presented to verify the effectiveness of the proposed control method. The co-simulations are implemented based on Matlab/Simulink–CarSim platform with a high-fidelity and full-vehicle model. The CarSim is a widely used dynamic software that can simulate and analyze the dynamic behavior of different vehicles in diversiform driving conditions. It incorporates a 27-degree-of-freedom full-vehicle model, which is equipped with nonlinear tyre models and virtual sensors as a standard feature (Jin, Yin, & Chen, 2015). In addition, various running conditions are simulated to test the effectiveness of the proposed method.

Table 1
Parameters related to the controller.

Symbol	Parameters	Value	Units
a	Distance from front axle to gravity center	1.192	m
b	Distance from rear axle to gravity center	1.598	m
x_p	Projected distance	5	m
J_z	Yaw inertia	2280	kg m^2
i	Steering ratio	18.5	null
C_{f0}	Nominal cornering stiffness of front-axle	57 810	N/rad
C_{r0}	Nominal cornering stiffness of rear-axle	67 810	N/rad
η	Strictly positive gain parameter	25	null
c_1	Strictly positive gain parameter	10	null
c_2	Strictly positive gain parameter	10	null
k_1	Positive gain parameter	500	null
k_2	Positive gain parameter	50	null
ρ	Learning rate	0.05	null
ζ	Momentum factor	0.5	null

A Gaussian distributed random signal filtered by low-pass filter is adopted, which is amplified i times as the equivalent random disturbance $d_e(\cdot)$, as shown by the purple curve in Figs. 8(f), 9(f) and 12(f). Under the conditions of low adhesion road at low speed and high adhesion road at high speed, the variances of random signal are set to 50 and 100, respectively.

In this paper, the proposed scheme with $d_e(\cdot)$, which means, when the proposed scheme is used, there is equivalent random disturbance $d_e(\cdot)$ in simulation and experiment. Similarly, the proposed scheme without $d_e(\cdot)$, which means the system is free from any disturbance in simulation and experiment.

4.1. Vehicle model verification

Emergency steering maneuver at or close to the driving limits is liable to cause the vehicle to spin out or even turn over, which are dangerous driving situations. For the sake of safety, a simulation research scheme is adopted in this study. However, the simulation research is credible only when the simulation model is valid. The following part is the validation process.

The scheme of vehicle model verification is shown in Fig. 4. In order to verify the accuracy and effectiveness of the model, both real-life test and simulation were conducted on a low adhesion road (μ = 0.2~0.4). As in Fig. 5, a Brilliance® experimental vehicle was used to test, and the parameters of the vehicle are given in Table 2 (see Appendix B). In test and simulation, the velocity input and the steering input are shown in Fig. 6. The real yaw rate, lateral acceleration and sideslip angle of vehicle are measured by gyroscope, acceleration sensor and differential global positioning system (DGPS) installed on a test vehicle, respectively (Ma, Liu, Ji, & Yang, 2017), and comparisons of responses between experiment and simulation are shown in Fig. 7. It can be seen that the responses of the experiment and those of the simulation are in good agreement, which indicates that the vehicle model is accurate and feasible. For the sideslip angle measuring and processing methods, the explanation is shown in Appendix C.

The results in Fig. 7(b) show that, the peak lateral accelerations of the experimental vehicle and the simulative one are both about −2.5 m/s^2. Hence, it can be inferred that, both the experimental and the simulative vehicles worked in the situation, which was very close to the adhesion limit (μg).

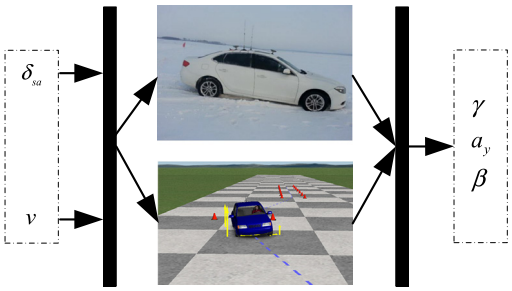

Fig. 4. The experimental verification scheme of the vehicle model.

Fig. 5. The test vehicle used for model verification.

4.2. Test on an ice snow covered pavement ($\mu = 0.3$)

Considering that the vehicle can easily become unstable as it makes a sharp turn on a low adhesion road, a double lane change maneuver is conducted on an ice snow-covered pavement with adhesion coefficient $\mu = 0.3$ and velocity $v = 54$ km/h to verify the effectiveness of the proposed lateral motion control scheme and simulate an emergency obstacle avoidance maneuver.

The results in Fig. 8(c) show that the peak lateral accelerations of vehicle controlled by the BVSC scheme, by the proposed schemes without $d_e(\cdot)$ and with $d_e(\cdot)$ are about -2.66 m/s^2, -2.65 m/s^2 and -2.65 m/s^2, respectively. Therefore, it can be inferred that, during the path tracking, in any of these schemes the vehicle operates in the situation which is very close to the tyre–road friction limit (μg).

As shown in Fig. 8(a), compared with the BVSC scheme, the proposed schemes, one without $d_e(\cdot)$ and one with $d_e(\cdot)$, both exhibit superior performance in tracking the reference path. It can be seen from Fig. 8(b) that, the peak values of lateral path tracking error for vehicle controlled by the BVSC scheme, by the proposed schemes without $d_e(\cdot)$ and with $d_e(\cdot)$ are about -0.13 m, -0.11 m and -0.11 m, respectively. It can be seen from Fig. 8(c), (d) and (e) that, the lateral accelerations, yaw rates and sideslip angles of the vehicle controlled by the proposed schemes with $d_e(\cdot)$ or without $d_e(\cdot)$ show better dynamic performance than the BVSC scheme. Fig. 8(a)–(e) show that, the proposed scheme can effectively resist against unknown external disturbance. In Fig. 8(f), it can easily be seen that, compared with the BVSC scheme, the peak values of steering angle in the proposed schemes without $d_e(\cdot)$ and with $d_e(\cdot)$ are smaller.

Fig. 8(g) and (h) give the test results of estimated cornering stiffness and estimated tyre lateral force, under the equivalent random disturbance $d_e(\cdot)$. Fig. 8(g) shows the cornering stiffness of the front-axle and the rear-axle, which are estimated by ANN approximator. It can be seen

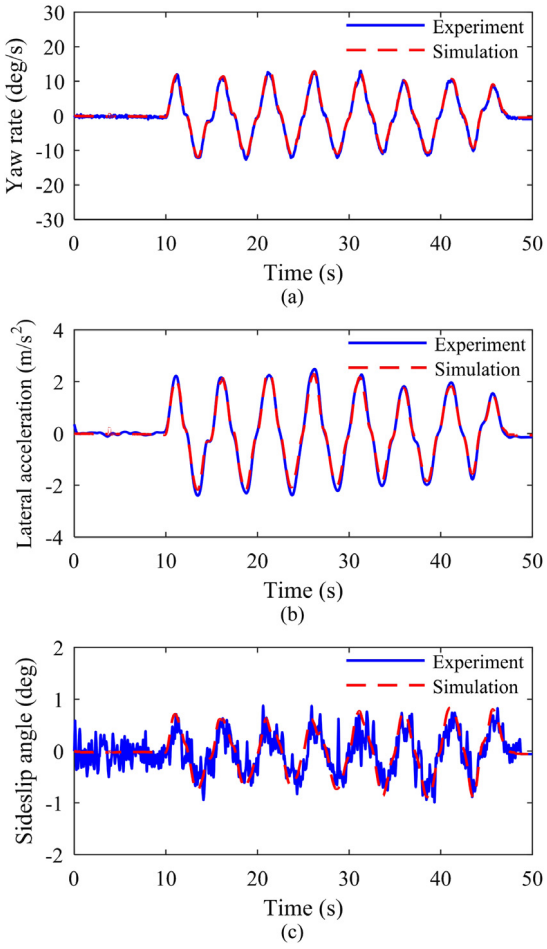

Fig. 7. Comparisons of responses between experiment and simulation. (a) Vehicle yaw rate, (b) vehicle lateral acceleration, (c) vehicle sideslip angle.

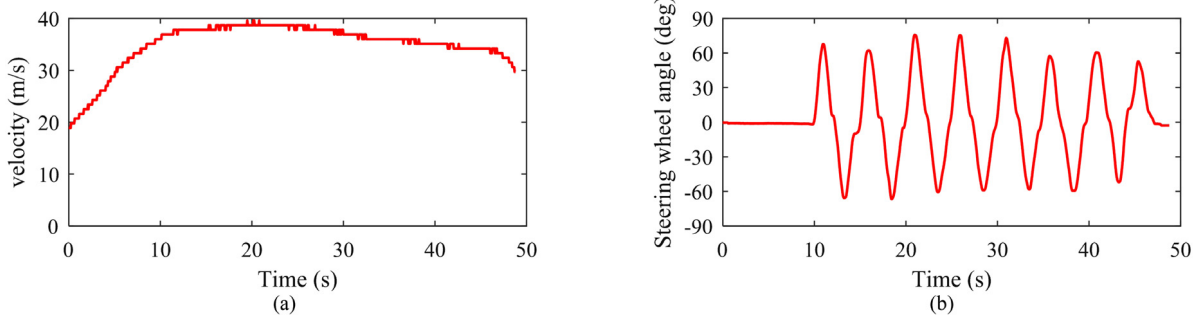

Fig. 6. Input signal. (a) Vehicle velocity, (b) steering wheel angle.

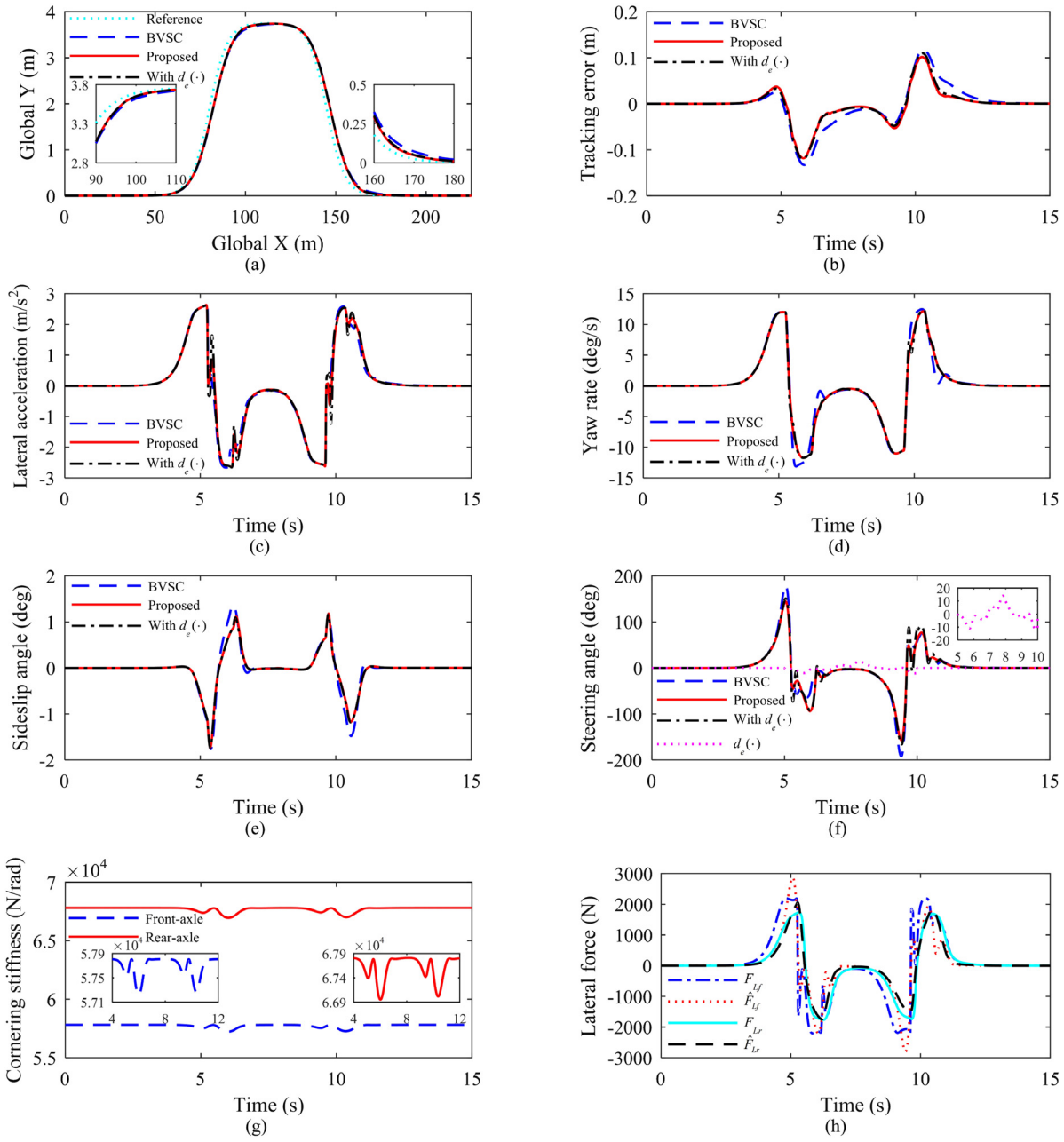

Fig. 8. The results of double lane change maneuver on an ice snow covered pavement ($\mu = 0.3$). (a) Global trajectory of the path following, (b) path tracking error, (c) vehicle lateral acceleration, (d) vehicle yaw rate, (e) vehicle sideslip angle, (f) control input for steering actuator and equivalent random disturbance, (g) estimated cornering stiffness of the front-axle and the rear-axle, (h) tyre lateral forces from Carsim and estimated tyre lateral forces for front-axle and rear-axle. (For interpretation of the references to color in this figure legend, the reader is referred to the web version of this article.)

that, the maximal amount of reduction are about 550 N/rad and 860 N/rad, respectively. As shown in Fig. 8(h), the estimated tyre lateral forces can acceptably converge to the tyre lateral forces from Carsim.

4.3. Test on a dry asphalt pavement ($\mu = 1.0$)

In order to further evaluate the performance of the proposed control method, considering that the vehicle can easily become unstable as it makes a sharp turn at high speed, a double lane change maneuver is carried out on a dry asphalt pavement with road adhesion coefficient $\mu = 1.0$ and velocity $v = 108$ km/h.

The results in Fig. 9(c) show that the peak lateral accelerations of vehicle controlled by the BVSC scheme, by proposed schemes without $d_e(\cdot)$ and with $d_e(\cdot)$ are about 8.25 m/s^2, 8.01 m/s^2 and 8.01 m/s^2, respectively. Meanwhile, it can also be found from Fig. 9(e) that, the tyres are highly saturated. Therefore, it can be inferred that, during the path tracking, the tyres of vehicle in the different schemes worked in their nonlinear region, and the autonomous vehicle operates at or close to its driving limits.

As shown in Fig. 9(a), compared with the BVSC scheme, the proposed schemes with $d_e(\cdot)$ or without $d_e(\cdot)$ show superior performance in tracking the reference path. Moreover, the peak values of lateral path tracking error in the BVSC scheme, in the proposed schemes without $d_e(\cdot)$ and with $d_e(\cdot)$ are about −1.42 m, −0.70 m and −0.70 m, respectively. Fig. 9(b) shows the peak values of heading error for vehicle controlled by the BVSC scheme, by the proposed schemes without $d_e(\cdot)$ and with $d_e(\cdot)$ are about 19.64°, 7.50° and 7.51°, respectively. It can be seen from Fig. 9(c), (d) and (e) that, the lateral acceleration, yaw rate and sideslip

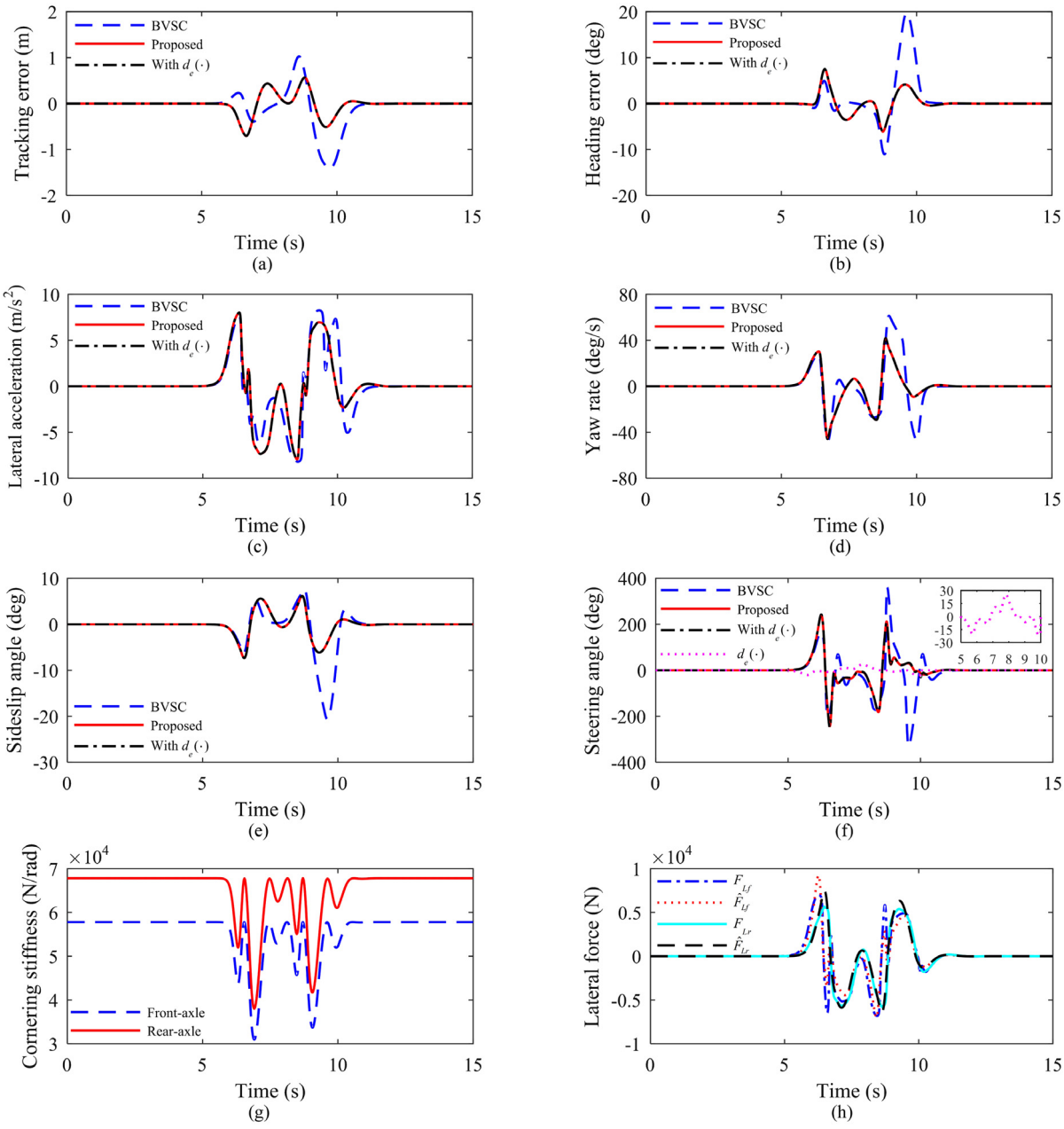

Fig. 9. The results of double lane change maneuver on a dry asphalt pavement ($\mu = 1.0$). (a) path tracking error, (b) heading error, (c) vehicle lateral acceleration, (d) vehicle yaw rate, (e) vehicle sideslip angle, (f) control input for steering actuator and equivalent random disturbance, (g) estimated cornering stiffness of the front-axle and the rear-axle, (h) tyre lateral forces from Carsim and estimated tyre lateral forces for front-axle and rear-axle. (For interpretation of the references to color in this figure legend, the reader is referred to the web version of this article.)

angle of the vehicle controlled by the proposed scheme shows better dynamic performance than the BVSC scheme. Fig. 9(a)–(e) show that, the proposed scheme can effectively resist against unknown external disturbance. In Fig. 9(f), it can easily be seen that there are more oscillations of the steering angle for the BVSC scheme, and compared with the BVSC scheme, the peak values of steering angle in the proposed scheme with $d_e(\cdot)$ or without $d_e(\cdot)$ are smaller.

Fig. 9(g) and (h) provide the test results of estimated cornering stiffness and estimated tyre lateral force, with the equivalent random disturbance $d_e(\cdot)$. Fig. 9(g) gives the cornering stiffness of front-axle and rear-axle, which are estimated by ANN approximator. It can be seen that, the cornering stiffness of front-axle and rear-axle decreases significantly during the path tracking, and the maximal amount of reduction are about 26 848 N/rad and 29 772 N/rad, respectively. As shown in Fig. 9(h), the estimated tyre lateral forces can acceptably converge to the tyre lateral forces from Carsim.

5. Experiment results with HIL system

An experiment using HIL system is conducted to test the real-time performance of the proposed control strategy. Fig. 10 shows the HIL system which consists mainly of a DS1501 MicroAutoBox from dSPACE®, a Freescale G36 actuator driver, a steer-by-wire system, a EXLAR electric servo cylinder for steering resistance loading, a BOSCH steering angular sensor, a NI® PXI hardware using LabVIEW, a monitor, a power supply, a terminal block, two host PCs and two displayers. Fig. 11 illustrates implementation architecture of the HIL system. In this system, vehicle–road system model of CarSim is encoded into PXI for real time testing. After obtaining the vehicle motion states from PXI,

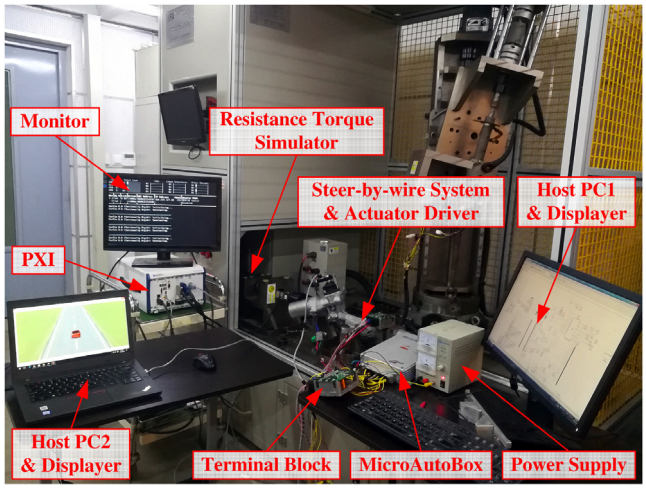

Fig. 10. HIL system for real-time testing.

the proposed controller, which is implemented in the MicroAutoBox, calculates the steering angle command of steer-by-wire system. Then the angle command is sent to the actuator driver to operate the steer-by-wire system, and the angular sensor feeds the values of corresponding steering column angle and angular speed back to nonlinear vehicle model of CarSim. The steering resistance torque, which is obtained from CarSim, acts on the rack of the steer-by-wire system by the EXLAR electric servo cylinder. The sampling rate of the experiments is 100 Hz.

In the HIL system, a double lane change maneuver is performed on an ice snow-covered pavement with friction coefficient $\mu = 0.3$ and velocity $v = 54$ km/h. The experiment results are shown in Fig. 12. It can be found that the results are similar to but not exactly the same as those given by CarSim–Simulink co-simulation. This is mainly because of communication delay and real characteristics of the electro-mechanical system.

The results in Fig. 12(c) show that the peak lateral accelerations of vehicle controlled by the BVSC scheme, by the proposed schemes without $d_e(\cdot)$ and with $d_e(\cdot)$, are about -2.60 m/s^2, -2.59 m/s^2 and -2.60 m/s^2, respectively. Therefore, it can be inferred that, during the path tracking, in any of these schemes the vehicle operates very close to the tyre–road friction limit (μg).

As shown in Fig. 12(a), compared with the BVSC scheme, the proposed schemes without $d_e(\cdot)$ and with $d_e(\cdot)$ show superior performance in tracking the reference path. In addition, the peak values of lateral path tracking error in the BVSC scheme, in the proposed schemes without $d_e(\cdot)$ and with $d_e(\cdot)$, are about -0.37 m, -0.35 m and -0.38 m, respectively. It can be seen from Fig. 12(b) that, the peak values of heading error for vehicle controlled by the BVSC scheme, by the proposed schemes without $d_e(\cdot)$ and with $d_e(\cdot)$ are about 2.96°, 2.79°and 2.96°, respectively. Fig. 12(c), (d) and (e) show that, the lateral acceleration, yaw rate and sideslip angle of the vehicle controlled by the proposed scheme show better dynamic performance than the BVSC scheme. Fig. 12(a)–(e) show that, the proposed scheme can effectively resist against unknown external disturbance. In Fig. 12(f), it can be seen that, the peak values of outputs from steer-by-wire system controlled by the BVSC scheme, by the proposed schemes without $d_e(\cdot)$ and with $d_e(\cdot)$ are about 82.29°, 74.62°and 75.92°, respectively.

Fig. 12(g) and (h) give the test results of estimated cornering stiffness and estimated tyre lateral force, under the equivalent random disturbance $d_e(\cdot)$. Fig. 12(g) shows the cornering stiffness of the front-axle and the rear-axle, which are estimated by ANN approximator. It can be found that, the maximal amount of reduction are about 671 N/rad and 1058 N/rad, respectively. As shown in Fig. 12(h), the estimated tyre lateral forces can acceptably converge to the tyre lateral forces from Carsim.

6. Conclusion

This paper proposes a novel lateral motion control scheme that maintains the yaw stability of autonomous vehicle while minimizing lateral path tracking deviation at the driving limits. In order to suppress lateral path tracking error and improve the robustness of the whole system, a robust steering controller is developed using the BVSC algorithm. An ANN approximator is designed to compensate the uncertainty of tyre cornering stiffness by learning to approximate arbitrary nonlinear functions, and it guarantees the uniform ultimate boundedness of the closed-loop system.

The results of co-simulation and experiment using the HIL system show that, with unknown external disturbance, the proposed method provides sufficient path tracking capability as well as yaw stability for autonomous vehicle at or close to the driving limits. Compared with the BVSC scheme, the proposed scheme shows superior lateral motion control performance, especially on dry asphalt pavement at high speed. In addition, the proposed strategy exhibits superior robustness to unknown external disturbances in different running conditions.

In future work, it is hoped that multi-object coordination equilibrium between vehicle stabilization and path tracking can be investigated by coordinated control of steering system and braking system.

Acknowledgments

The authors greatly appreciate the support from the National Natural Science Foundation of China (grant numbers U1664263, 51375009), the Independent Research Program of Tsinghua University (grant number 20161080033), and the Natural Science Foundation of Shandong Province (grant numbers ZR2016EEQ06).

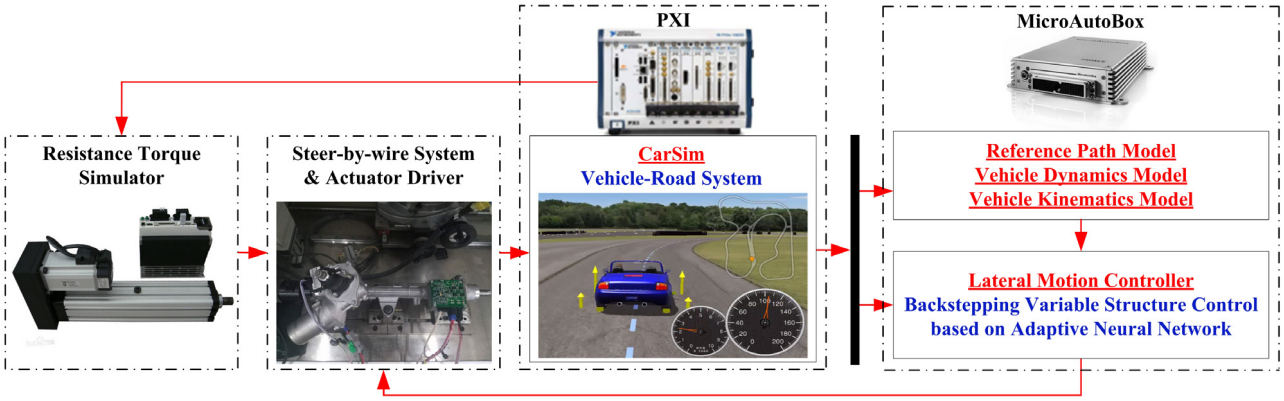

Fig. 11. Implementation architecture of the HIL system.

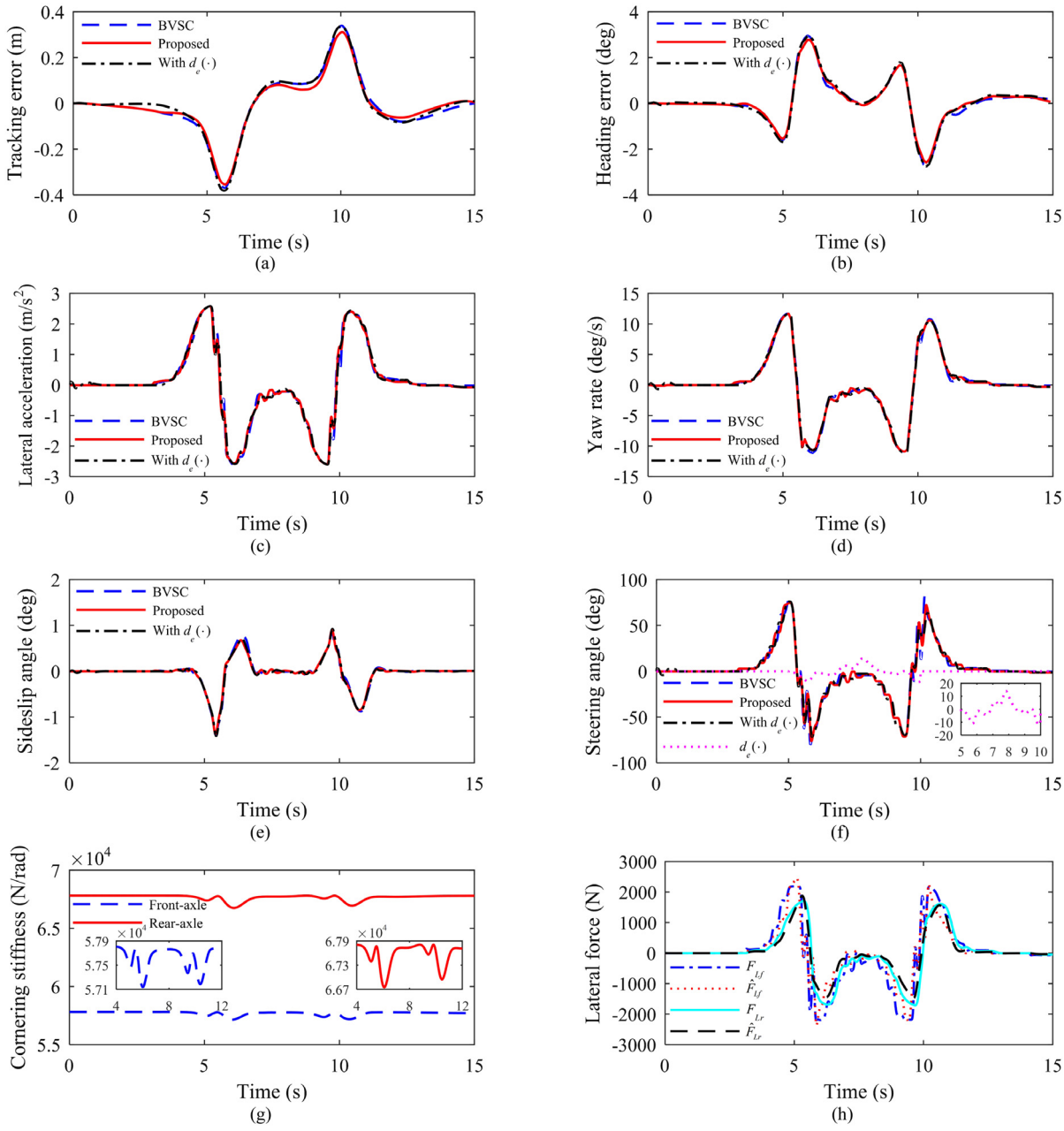

Fig. 12. The experimental results of double lane change maneuver on an ice snow covered pavement ($\mu = 0.3$). (a) path tracking error, (b) heading error, (c) vehicle lateral acceleration, (d) vehicle yaw rate, (e) vehicle sideslip angle, (f) output of steer-by-wire system and equivalent random disturbance, (g) estimated cornering stiffness of the front-axle and the rear-axle, (h) tyre lateral forces from Carsim and estimated tyre lateral forces for front-axle and rear-axle. (For interpretation of the references to color in this figure legend, the reader is referred to the web version of this article.)

Appendix A

From the mathematical definition of the tanh(.) function, and for every given scalar x, the following equation can be obtained:

$$x\tanh(x) = x\frac{e^{x} - e^{-x}}{e^{x} + e^{-x}} = \frac{1}{e^{2x}+1}x\left(e^{2x}-1\right), \tag{A.1}$$

where

$$\begin{cases} e^{2x} - 1 \geq 0, & x \geq 0 \\ e^{2x} - 1 < 0, & x < 0. \end{cases} \tag{A.2}$$

According to (A.2), the following relation is derived:

$$x\left(e^{2x}-1\right) \geq 0. \tag{A.3}$$

Hence, a conclusion can be obtained:

$$x\tanh(x) = \frac{1}{e^{2x}+1}x\left(e^{2x}-1\right) \geq 0. \tag{A.4}$$

Appendix B

The vehicle model is calibrated against the Brilliance® vehicle, and the parameters of the vehicle model are given in Table 2.

Appendix C

The sideslip angle of vehicle is obtained by the angle between longitudinal velocity and east direction θ_a, and the angle between the velocity and north direction θ_b, as illustrated in Fig. C.1.

A and B represent two mobile stations installed on the experimental vehicle which receive the data transferred from base station and satellite

Table 2
Main parameters of the vehicle model.

Symbol	Parameter	Value	Units
m	Vehicle mass	1528.13	kg
m_s	Vehicle sprung mass	1368.13	kg
m_{us}	Vehicle unsprung mass	160	kg
a	Distance from front axle to gravity center	1.192	m
b	Distance from rear axle to gravity center	1.598	m
B_f, B_r	Track width of front and rear axle	1.565	m
h_c	Height of gravity center	0.506	m
I_{sprung_xx}	Moment of inertia of sprung mass - roll	628	kg m^2
I_{sprung_yy}	Moment of inertia of sprung mass - pitch	1958	kg m^2
J_z	Moment of inertia of sprung mass - yaw	2280	kg m^2
I_{sprung_xy}	Product of inertia of sprung mass - *Ixy*	0	kg m^2
I_{sprung_xz}	Product of inertia of sprung mass - *Ixz*	−8.168	kg m^2
I_{sprung_yz}	Product of inertia of sprung mass - *Iyz*	0	kg m^2
K_{susp_front}	Suspension stiffness (front axle)	21 000	N/m
K_{susp_rear}	Suspension stiffness (rear axle)	21 000	N/m
R_{susp_front}	Suspension damping (front axle)	2000	N/(m/s)
R_{susp_rear}	Suspension damping (rear axle)	1500	N/(m/s) s
$K_{antiroll\_front}$	Antiroll bar stiffness (front axle)	30 000	Nm/rad
$K_{antiroll\_rear}$	Antiroll bar stiffness (rear axle)	20 000	Nm/rad
R_{free}	Free radius of the tyre	0.307	m
i_{sw}	Steering gear ratio	18.5	

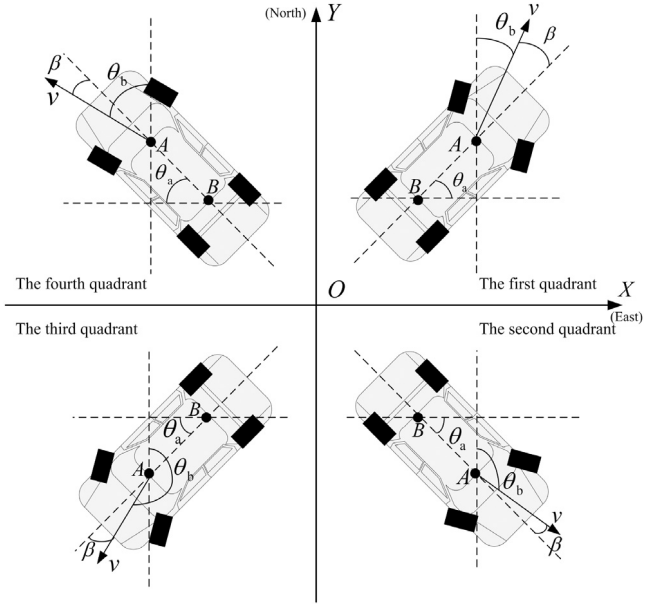

Fig. C.1. The schematic of calculating method of sideslip angle.

(Li, Chen et al., 2014; Li, Jia, Ran, Song, & Wu, 2014). The angle θ_b is obtained directly from the DGPS, and θ_a is calculated by Eq. (C.5) as follows

$$\theta_a = \arctan \frac{\left|y'_a - y'_b\right|}{\left|x'_a - x'_b\right|}, \tag{C.5}$$

where (x'_a, y'_a) and (x'_b, y'_b) are the positions relative to the original position which is the absolute position at $t = 0$ in Gauss coordinate.

If the direction of velocity is at the left of AB line, the sideslip angle of vehicle is calculated by Eq. (C.6), otherwise it is calculated by Eq. (C.7).

$$\begin{cases} \beta = \dfrac{\pi}{2} - \theta_a - \theta_b, \text{the first quadrant} \\ \beta = \dfrac{\pi}{2} + \theta_a - \theta_b, \text{the second quadrant} \\ \beta = \dfrac{3\pi}{2} - \theta_a - \theta_b, \text{the third quadrant} \\ \beta = \dfrac{3\pi}{2} + \theta_a - \theta_b, \text{the fourth quadrant} \end{cases}. \tag{C.6}$$

$$\begin{cases} \beta = \theta_b - \dfrac{\pi}{2} + \theta_a, \text{the first quadrant} \\ \beta = \theta_b - \dfrac{\pi}{2} - \theta_a, \text{the second quadrant} \\ \beta = \theta_b - \dfrac{3\pi}{2} + \theta_a, \text{the third quadrant} \\ \beta = \theta_b - \dfrac{3\pi}{2} - \theta_a, \text{the fourth quadrant} \end{cases}. \tag{C.7}$$

In the experimental data processing of sideslip angle, the Butterworth low-pass filter is adopted, the filter order is set to 4, and the passband edge frequency is set to 30 rad/s.

References

Brown, M., Funke, J., Erlien, S., & Gerdes, J. C. (2017). Safe driving envelopes for path tracking in autonomous vehicles. *Control Engineering Practice*, *61*, 307–316.

Chen, Y., & Wang, J. (2011). Adaptive vehicle speed control with input injections for longitudinal motion independent road frictional condition estimation. *IEEE Transactions on Vehicular Technology*, *60*(3), 839–848.

Coban, R. (2017). Dynamical adaptive integral backstepping variable structure controller design for uncertain systems and experimental application. *International Journal of Robust and Nonlinear Control*.

Eskandarian, A. (2012). *Handbook of intelligent vehicles*. Springer.

Falcone, P., Borrelli, F., Asgari, J., Tseng, H. E., & Hrovat, D. (2007). Predictive active steering control for autonomous vehicle systems. *IEEE Transactions on Control Systems Technology*, *15*(3), 566–580.

Fei, J., & Ding, H. (2012). Adaptive sliding mode control of dynamic system using rbf neural network. *Nonlinear Dynamics*, *70*(2), 1563–1573.

Funke, J., Brown, M., Erlien, S. M., & Gerdes, J. C. (2017). Collision avoidance and stabilization for autonomous vehicles in emergency scenarios. *IEEE Transactions on Control Systems Technology*, *25*(4), 1204–1216.

Gao, Y., Gray, A., Carvalho, A., Tseng, H. E., & Borrelli, F. (2014). Robust nonlinear predictive control for semiautonomous ground vehicles. In *Proceedings IEEE international conference american control conference* (pp. 4913–4918).

Gao, Y., Gray, A., Tseng, H. E., & Borrelli, F. (2014). A tube-based robust nonlinear predictive control approach to semiautonomous ground vehicles. *Vehicle System Dynamics*, *52*(6), 802–823.

González, D., Pérez, J., Milanés, V., & Nashashibi, F. (2016). A review of motion planning techniques for automated vehicles. *IEEE Transactions on Intelligent Transportation Systems*, *17*(4), 1135–1145.

Guo, H., Liu, J., Cao, D., Chen, H., Yu, R., & Lv, C. (2017). Dual-envelop-oriented moving horizon path tracking control for fully automated vehicles. *Mechatronics*, 1–12.

Guo, J., Hu, P., Li, L., & Wang, R. (2012). Design of automatic steering controller for trajectory tracking of unmanned vehicles using genetic algorithms. *IEEE Transactions on Vehicular Technology*, *61*(7), 2913–2924.

Hang, P., Chen, X., Luo, F., & Fang, S. (2017). Robust control of a four-wheel-independent-steering electric vehicle for path tracking. *SAE International Journal of Vehicle Dynamics, Stability, and NVH*, *1*, (2017-01-1584).

Hashemi, E., Khosravani, S., Khajepour, A., Kasaiezadeh, A., Chen, S. K., & Litkouhi, B. (2017). Longitudinal vehicle state estimation using nonlinear and parameter-varying observers. *Mechatronics*, *43*, 28–39.

He, W., Chen, Y., & Yin, Z. (2016). Adaptive neural network control of an uncertain robot with full-state constraints. *IEEE Transactions on Cybernetics*, *46*(3), 620–629.

He, X., Yang, K., Ji, X., Liu, Y., & Deng, W. (2017). Research on Vehicle Stability Control Strategy Based on Integrated-Electro-Hydraulic Brake System. WCX™ 17: SAE World Congress Experience, Apr: 2017-01-1565.

Hu, C., Jing, H., Wang, R., Yan, F., & Chadli, M. (2016). Robust H_∞ output-feedback control for path following of autonomous ground vehicles. *Mechanical Systems and Signal Processing*, *70–71*, 414–427.

Hwang, C. L., Yang, C. C., & Hung, J. Y. (2017). Path tracking of an automatic ground vehicle with different payloads by hierarchical improved fuzzy dynamic sliding-mode control. *IEEE Transactions on Fuzzy Systems*.

Ji, J., Khajepour, A., Melek, W. W., & Huang, Y. (2017). Path planning and tracking for vehicle collision avoidance based on model predictive control with multiconstraints. *IEEE Transactions on Vehicular Technology*, *66*(2), 952–964.

Jin, X. J., Yin, G., & Chen, N. (2015). Gain-scheduled robust control for lateral stability of four-wheel-independent-drive electric vehicles via linear parameter-varying technique. *Mechatronics*, *30*, 286–296.

Kapania, N. R., & Gerdes, J. C. (2015). Design of a feedback-feedforward steering controller for accurate path tracking and stability at the limits of handling. *Vehicle System Dynamics*, *53*(12), 1687–1704.

Kim, W., Son, Y. S., & Chung, C. C. (2016). Torque-overlay-based robust steering wheel angle control of electrical power steering for a lane-keeping system of automated vehicles. *IEEE Transactions on Vehicular Technology*, *65*(6), 4379–4392.

Kritayakirana, K., & Gerdes, J. C. (2012a). Using the centre of percussion to design a steering controller for an autonomous race car. *Vehicle System Dynamics*, *50*(Suppl. 1), 33–51.

Kritayakirana, K., & Gerdes, J. C. (2012b). Autonomous vehicle control at the limits of handling. *International Journal of Vehicle Autonomous Systems*, *10*(4), 271–296.

Lam, A. Y., Leung, Y. W., & Chu, X. (2016). Autonomous-vehicle public transportation system: scheduling and admission control. *IEEE Transactions on Intelligent Transportation Systems*, *17*(5), 1210–1226.

Laurense, V. A., Goh, J. Y., & Gerdes, J. C. (2017). Path-tracking for autonomous vehicles at the limit of friction. In *Proceedings IEEE international conference american control conference* (pp. 5586-5591).

Lee, J., Choi, J., Yi, K., Shin, M., & Ko, B. (2014). Lane-keeping assistance control algorithm using differential braking to prevent unintended lane departures. *Control Engineering Practice*, *23*, 1–13.

Lefèvre, S., Carvalho, A., & Borrelli, F. (2016). A learning-based framework for velocity control in autonomous driving. *IEEE Transactions on Automation Science and Engineering*, *13*(1), 32–42.

Li, Q., Chen, L., Li, M., Shaw, S. L., & Nuchter, A. (2014). A sensor-fusion drivable-region and lane-detection system for autonomous vehicle navigation in challenging road scenarios. *IEEE Transactions on Vehicular Technology*, *63*(2), 540–555.

Li, L., Jia, G., Ran, X., Song, J., & Wu, K. (2014). A variable structure extended kalman filter for vehicle sideslip angle estimation on a low friction road. *Vehicle System Dynamics*, *52*(2), 280–308.

Liu, J. (2013). Radial Basis Function (RBF) neural network control for mechanical systems: design, analysis and Matlab simulation. Springer.

Liu, Y., Fan, X., Lv, C., et al. (2018). An innovative information fusion method with adaptive Kalman filter for integrated INS/GPS navigation of autonomous vehicles. *Mechanical Systems and Signal Processing*, *100*, 605–616.

Liu, Y. H., Li, T., Yang, Y. Y., Ji, X. W., & Wu, J. (2017). Estimation of tyre-road friction coefficient based on combined APF-IEKF and iteration algorithm. *Mechanical Systems and Signal Processing*, *88*, 25–35.

Ma, B., Liu, Y., Gao, Y., Yang, Y., Ji, X., & Bo, Y. (2016). Estimation of vehicle sideslip angle based on steering torque. *The International Journal of Advanced Manufacturing Technology*, 1–9.

Ma, B., Liu, Y., Ji, X., & Yang, Y. (2017). Investigation of a steering defect and its compensation using a steering-torque control strategy in an extreme driving situation. *Proceedings of the Institution of Mechanical Engineers, Part D: Journal of Automobile Engineering*.

Ni, J., & Hu, J. (2017). Dynamics control of autonomous vehicle at driving limits and experiment on an autonomous formula racing car. *Mechanical Systems and Signal Processing*, *90*, 154–174.

Ostafew, C. J., Schoellig, A. P., & Barfoot, T. D. (2016). Robust Constrained Learning-based NMPC enabling reliable mobile robot path tracking. *International Journal of Robotics Research*, *35*(13), 1547–1563.

Petrov, P., & Nashashibi, F. (2014). Modeling and nonlinear adaptive control for autonomous vehicle overtaking. *IEEE Transactions on Intelligent Transportation Systems*, *15*(4), 1643–1656.

Piltan, F., Mansoorzadeh, M., Zare, S., Shahryarzadeh, F., & Akbari, M. (2013). Artificial tune of fuel ratio: Design a novel siso fuzzy backstepping adaptive variable structure control. *International Journal of Electrical and Computer Engineering*, *3*(2), 171–185.

Rosolia, U., Carvalho, A., & Borrelli, F. (2017). Autonomous Racing using Learning Model Predictive Control. In *Proceedings IEEE international conference American control conference* (pp. 5115–5120).

Tan, D., Chen, W., Wang, H., & Gao, Z. (2017). Shared control for lane departure prevention based on the safe envelope of steering wheel angle. *Control Engineering Practice*, *64*, 15–26.

Thomas, P., Morris, A., Talbot, R., & Fagerlind, H. (2013). Identifying the causes of road crashes in Europe. *Annals of Advances in Automotive Medicine*, *57*, 13–22.

Wang, R., Hu, C., Yan, F., & Chadli, M. (2016). Composite nonlinear feedback control for path following of four-wheel independently actuated autonomous ground vehicles. *IEEE Transactions on Intelligent Transportation Systems*, *17*(7), 2063–2074.

World Health Organization, (2015). Top 10 causes of death worldwide. Retrieved from http://www.who.int/mediacentre/factsheets/fs310/en/. (Accessed July 2017).

Xia, Y., Pu, F., Li, S., & Gao, Y. (2016). Lateral path tracking control of autonomous land vehicle based on ADRC and differential flatness. *IEEE Transactions on Industrial Electronics*, *63*(5), 3091–3099.

Yu, R., Guo, H., Sun, Z., & Chen, H. (2015). MPC-based regional path tracking controller design for autonomous ground vehicles. In *Proceedings IEEE international conference systems, man, and cybernetics* (pp. 2510–2515).

Zhang, H., & Wang, J. (2017). Active steering actuator fault detection for an automatically-steered electric ground vehicle. *IEEE Transactions on Vehicular Technology*, *66*(5), 3685–3702.

Zhu, Q., Huang, Z., Liu, D., & Dai, B. (2016). An adaptive path tracking method for autonomous land vehicle based on neural dynamic programming. In *Proceedings IEEE international conference mechatronics and automation* (pp. 1429–1434).